

EXPLORING CRYOGENIC PROPELLANT BEHAVIOR IN LOW-GRAVITY ENVIRONMENTS, INSIGHTS FROM THE SATURN AS-203 VENT EXPERIMENTS AND CFD ANALYSIS

Justin Pesich,^{*} and Daniel Hauser[†]

In the 1960s, NASA embarked on a series of groundbreaking flight tests on the Saturn AS-203, aiming to understand the complex dynamics of propellants in the distinctive low-gravity lunar environment. These tests centered on venting experiments, subjecting cryogenic liquid hydrogen to conditions beneath its saturation pressure while accelerating the vehicle to manage the propellant's positioning.

During these experiments, NASA meticulously scrutinized the propellant tank using a suite of instruments, including temperature and pressure sensors, as well as a camera placed internal to the liquid hydrogen tank. The outcomes provided anecdotal evidence revealing the phenomenon of boiling along the tank's walls and the intriguing formation of liquid globules and droplets in the ullage during the venting process. Notably, the substantial drop in liquid temperature during these tests suggests adiabatic cooling as liquid hydrogen evaporates. This evaporation leads to a cooling of the remaining hydrogen due to the heat it releases.

This paper presents the outcomes of our initial analysis, wherein CFD models were used to simulate the observed boiling phenomena and the bulk movement of the liquid hydrogen propellant, both qualitatively and quantitatively. The implications of these findings may extend to mission and vehicle designers, providing invaluable insights for crafting more efficient and effective in-space propulsion systems utilizing cryogenic propellant including impacts to vehicle control systems. Understanding propellant behavior under these conditions may better inform GNC teams, ensuring more stable vehicle operations when utilizing cryogenic propellants. This includes essential considerations for cryogenic propellant transfer and storage systems, integral to NASA's forthcoming Artemis missions. While we recognize the challenges tied to CFD models, this study represents a step forward, highlighting current progress and signaling the potential for refining our predictive understanding in the future.

INTRODUCTION

In the 1960's during NASA's planned manned missions to the moon, there was uncertainty on how cryogenic propellants crucial for the mission would behave in low gravity environments. As a result, NASA conducted an important test flight using the flight vehicle Saturn AS-203¹. The mission tested several operations to determine how the cryogenic propellant, particularly liquid hydrogen (LH2), would behave. A pivotal aspect of the test flight was to observe the thermodynamic behavior when the internal pressure was modulated to fall beneath the liquid hydrogen's

^{*} Cryogenic Fluid Systems Engineer, Propulsion Division, NASA Glenn Research Center, 21000 Brookpark Rd, Cleveland, OH 44135.

[†] Cryogenic Fluid Systems Engineer, Propulsion Division, NASA Glenn Research Center, 21000 Brookpark Rd, Cleveland, OH 44135.

saturation pressure at controlled low accelerations. This experiment aimed to quantify the propellants level fluctuation consequently to boiling in a state of superheat. The bubbles that are generated at the wall and within the liquid slowly rise to the reduced buoyancy forces acting on them in low gravity.

Concurrently, NASA, in collaboration with industry partners, engineering sophisticated theoretical models to predict the ascent of the liquid level in the tank². Data from three distinct venting tests, where pressure was decreased below the saturation pressure, revealed minimal changes in the liquid hydrogens level, corroborating the predictive models which estimated the relative fill level changes to range from 5-15%.

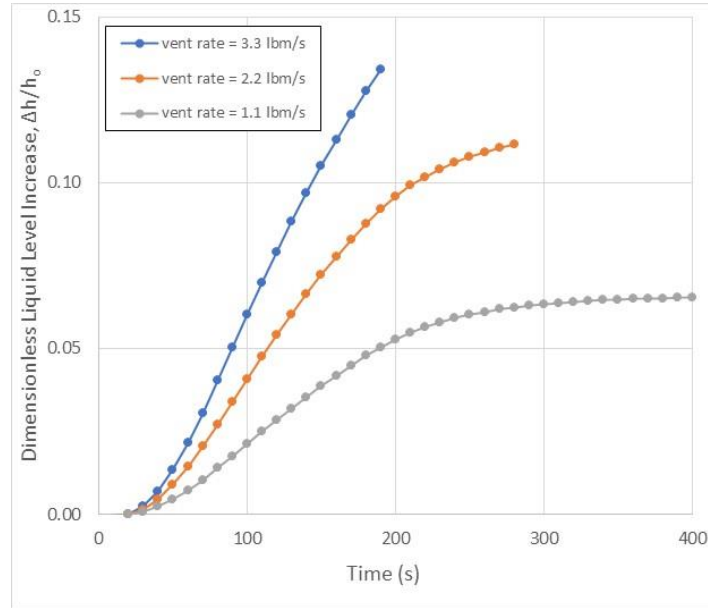


Figure 1. Predicted Liquid Hydrogen Relative Fill Level Change

Notably, the vent test conducted at fill levels below 50% manifested a less than 15% variation in fill level had negligible impact at half capacity but presents critical concerns at higher fill levels, particularly above 80-90%. A scenario where the tank, nearly full with 90% liquid undergoes venting introduces the risk of surpassing the tanks capacity and potentially ejecting valuable propellant and imparting operational efficiency. Moreover, such conditions may precipitate control stabilities within the spacecraft. The ejection of a bi-phasic mixture via non-thrust vents disrupts the uniformity of the mass ejection, possibly inducing an asymmetrical force distribution that could compromise the vehicles stability. These insights underscore the importance of precise fluid management in spacecraft design and operation.

Modern Computational Fluid Dynamic (CFD) tools were explored to determine the tools capabilities at predicting the two-phase processes that occur within a cryogenic propellant tank when the pressure is decreased below the saturation pressure of the liquid. The commercial CFD code STAR-CCM³ was selected to be used due to its advanced capabilities with predicting boiling processes. The volume-of-fluid numerical method within STAR-CCM was selected due to its simulation speed.

SATURN AS 203 EXPERIMENT OVERVIEW

The Saturn AS-203 flight test results are reported in NASA Contractor Report NASA-CR-94045¹. Propellant tank analytical models were developed and computations of the Saturn AS-203 flight experiments were performed and documented in NASA Contractor Report NASA-CR-109847². The tank depressurization test consisted of three LH2 tank blowdowns using a non-propulsive vent (NPV) system illustrated in Figure 2. The details of each blowdown are presented in Table 1. Note that some test details in Reference 1 and Reference 2 do not agree, so the test details reported herein are from Reference 2. Note that all three blowdowns used the NPV system states the first blowdown used the continuous vent system. This is because it groups the second and third blowdowns into one, and the naming convention is changed here for clarity. The first blowdown was selected for model validation.

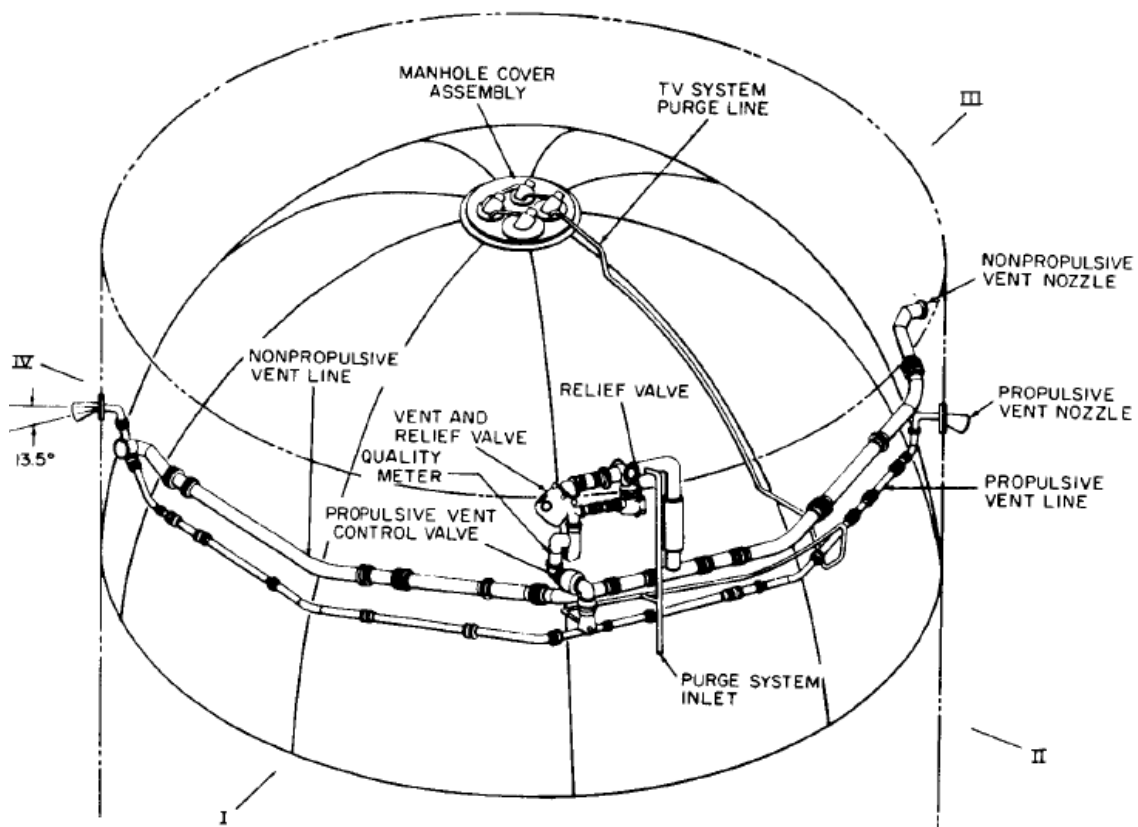


Figure 2. Saturn AS-203 Vent System Schematic (not pictured: vent piping tank egress near top dead center)¹

Table 1. Vent test details.³

Test Detail	First Blowdown	Second Blowdown	Third Blowdown
NPV Open (seconds after liftoff)	14342.2	16723.2	17023.2
NPV Close (seconds after liftoff)	14522.2	16813.2	17113.2
Duration (seconds)	180	90	90
Initial Pressure (psia)	19.5	17.0	14.4
Final Pressure (psia)	13.8	13.0	11.9
Estimated Vented Mass (lb)	360	150	160

The vehicle acceleration, heat loads on the hydrogen tank walls, and mass flow rate from the NPV system were all measured over the entire mission duration and will be discussed in a later section as model boundary conditions. The settling acceleration was maintained by thrusting from both the LH2 continuous vent system and the liquid oxygen (LOX) ullage thrust valve for the duration of the first blowdown and was on the order of 10^{-3} m/s/s. Only the LH2 continuous vent system was used to settle for the second and third blowdowns and was on the order of 10^{-4} m/s/s. The applied settling thrust is required to keep the liquid aft in the tank and avoid venting valuable liquid hydrogen. As you apply any force to the vehicle, the trajectory of the vehicle is compromised and will have an affect on Guidance, Navigation and Control (GN&C) of the spacecraft. Thus, it is important to understand the effect of liquid level rise due to venting a cryogenic boiling tank, and the settling thrust required to limit the liquid level rise. In addition, if liquid hydrogen is vented through non-propulsive vent hardware, it could provide unexpected forces on the vehicle that will affect GN&C inputs.

Prior to the first blowdown, the internal tank video camera showed the liquid settled in the bottom of the tank. The temperature sensors indicated the liquid was saturated. Reference 1 indicated the ullage was superheated under nearly steady-state continuous venting conditions, whereas Reference 2 stated the ullage was saturated throughout. Once the NPV system was opened, a white fog formed that obscured the liquid-vapor interface (LVI). Nearly spherical liquid particles, roughly 1-6 inches in diameter, were seen floating in the ullage 135 seconds into the blowdown. It is suspected that bulk boiling occurred at small nucleation sites on sensors or tank internals. The liquid superheat, due to venting the ullage down below the saturation pressure, caused rapid bubble growth and could have thrown liquid at the liquid-vapor interface into the ullage.

CFD MODEL

Geometry

The computational domain was defined by a 3D 30-degree sector of the Saturn AS-203 hydrogen fuel tank displayed in Figure 3. The tank wall boundaries are specified in Figure 4. The geometry includes the tank interior and solid tank wall to account for the conjugate heat transfer. The solid tank wall was assumed to have a uniform thickness of 1 mm. The vent outlet was assumed to

be on the tank centerline near the forward dome. Although the vent outlet was slightly off-center in the test hardware, it was moved to the centerline to accommodate axisymmetric simulation assumptions. Other than the slosh baffle and deflector, no tank internals were modeled (instrumentation rakes, struts, helium tanks, etc.). Notable tank geometry dimensions are given in Table 2.

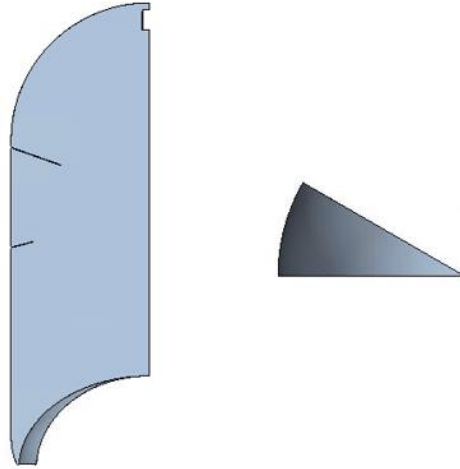


Figure 3. Computational Model Geometry Side View (left) and Top View (right) of a 30-Degree Sector

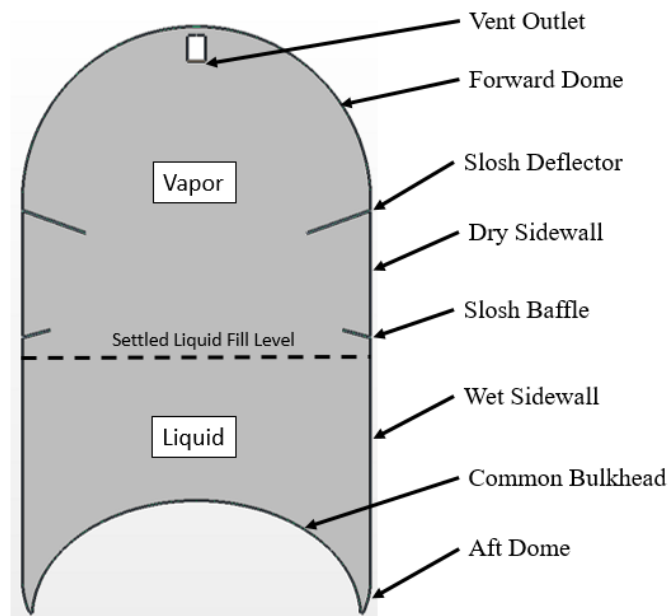


Figure 4. Tank Wall Boundaries

Table 2. LH2 Tank Geometry Dimensions.

Dimension	Value
Tank Height (m)	11.320
Tank Diameter (m)	6.630
Vent Pipe Diameter (m)	0.168

Computational Mesh

Two meshes were created to assess mesh independence and are presented in Figure 5 on one of the two periodic interfaces of the sector. A zoomed-in view near where the wall, slosh baffle, and LVI meet is also provided. The fine mesh refined the mesh size on the wet sidewall, at the LVI, and used a finer boundary layer grid using more prism layers on the wet sidewall. In addition, a new annular refinement was applied near the wall where bubbles would form, grow, coalesce, and detach moving upwards to the LVI. To keep the fine mesh of reasonable size, the dry wall cell size was coarsened and the bulk mesh in the liquid and vapor was allowed to grow to a larger size, compared to the coarse mesh. The total cell counts for each mesh is listed in Table 3.

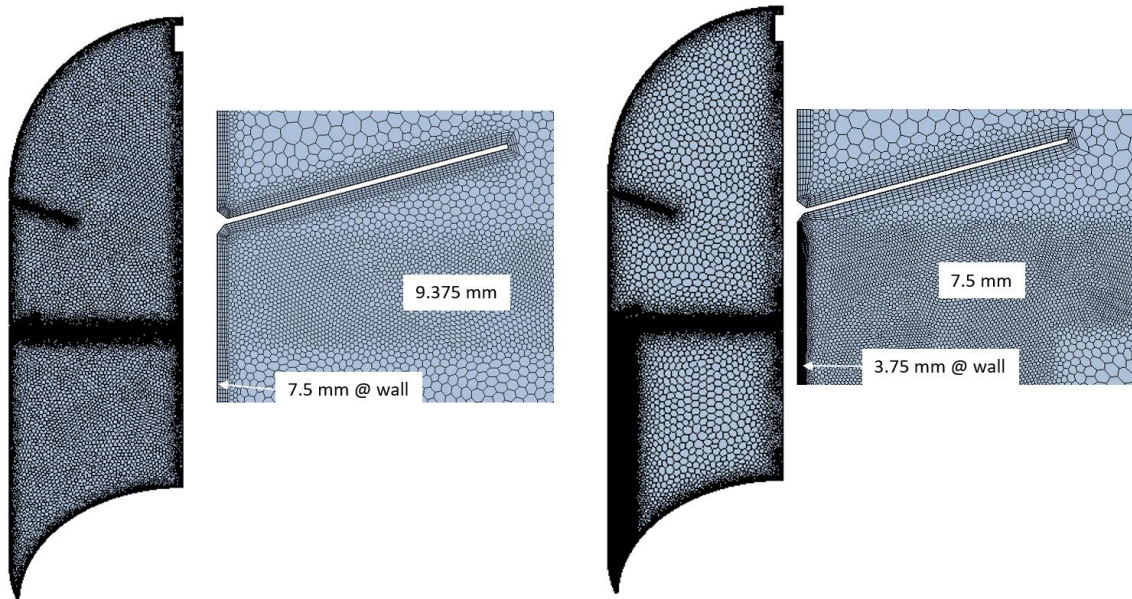


Figure 5. Coarse Mesh (left) and Fine Mesh (right) Comparison.

Table 3. Mesh Sizes.

Mesh	Total Cell Count
Coarse	~7 million
Fine	~31 million

Initial Conditions and Boundary Conditions

The liquid level during the test was reported to be approximately six inches below the baffle, resulting in an approximate liquid fill level of 44% by volume². The liquid and vapor were assumed to be quiescent prior to venting so the initial velocity was set to zero. The initial pressure was set to the experimentally measured tank pressure at the beginning of the first blowdown of 19.5 psia (see Table 1). The initial temperature was set to the saturation temperature for hydrogen corresponding to a pressure of 19.5 psia and was uniform throughout the tank model including the solid tank wall. The ullage superheat and stratification was unclear between Reference 1 and Reference 2. For simplicity, a constant value was used throughout the fluid domain. A sensitivity study to ullage superheat could be performed at a later date. Turbulence model initial conditions were left at the default values. The turbulence intensity was set to 0.01, the turbulent velocity scale was set to 1.0 m/s, and the turbulent viscosity ratio was set to 10.

Since a 30-degree sector of the tank was modeled, the two boundaries forming the wedge that intersect at the tank centerline axis were defined as periodic interfaces. The vent outlet was set to a constant mass flow rate using the average of the mass flow rate measured in the NPV system throughout the first blowdown, where the experimental data is shown in Figure 6. Note that the vent flow rate is the value extracted from the test data and was scaled down by 30/360 to account for the reduced domain size. The measured heat loads were applied to the outer solid wall of each boundary as a time-dependent boundary condition shown in Figure 7. The vehicle acceleration also varied over time and was approximated by a linear function shown in Figure 8. The negative acceleration corresponds to settling propellant aft. Test data were extracted by digitizing the figures in the experiment reports. All internal tank walls were assigned a no-slip viscous condition.

The constants used for initial conditions and boundary conditions are given in Table 4.

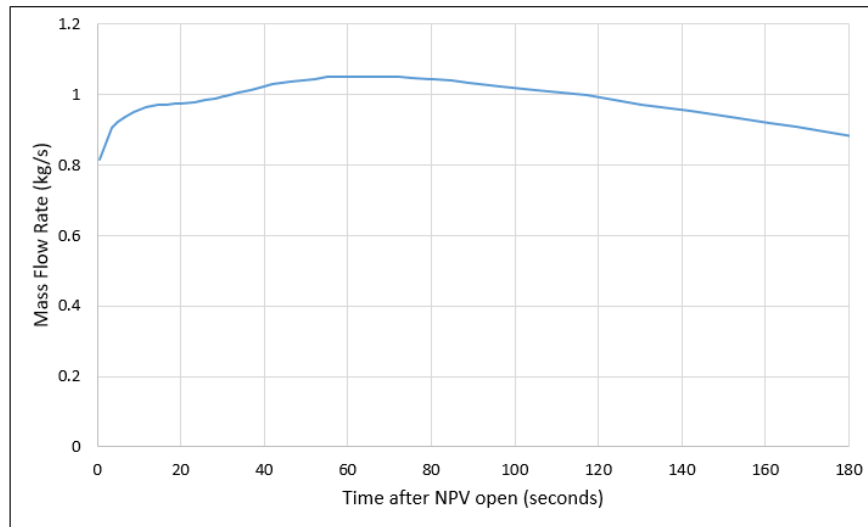


Figure 6. Measured Vent Flow Rate During First Blowdown.¹

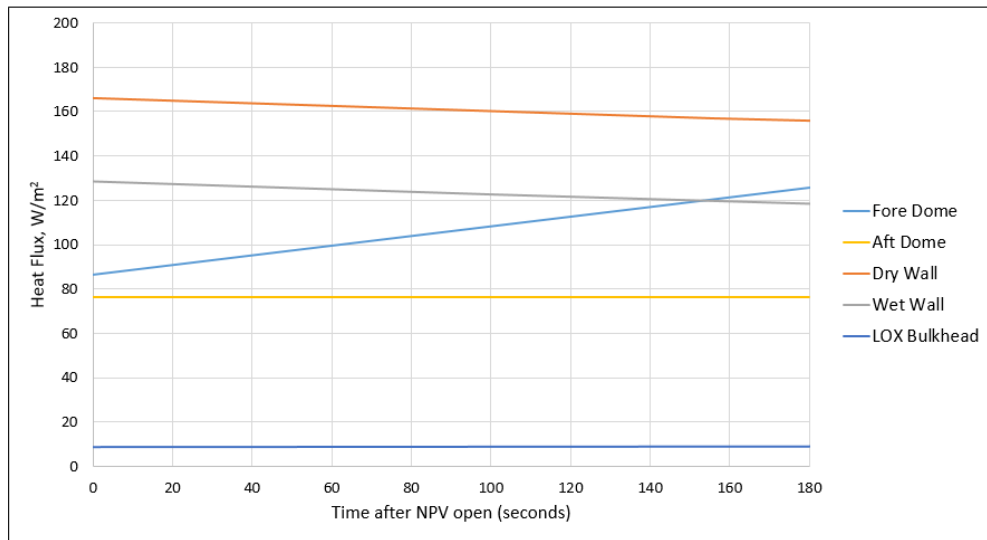


Figure 7. Measured Heat Loads During First Blowdown.

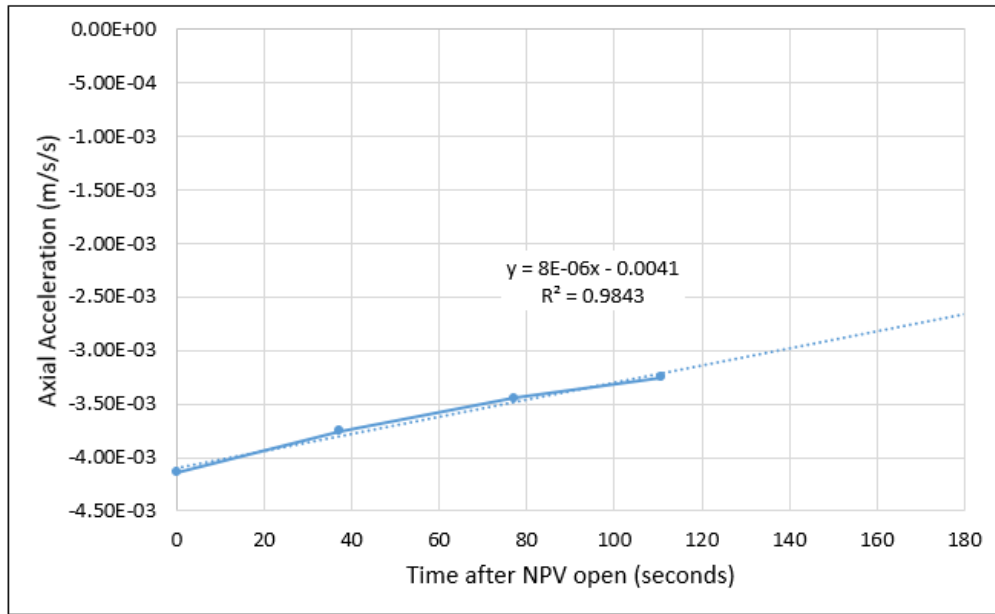


Figure 8. Measured Vehicle Acceleration During First Blowdown.

Table 4. Constant Initial Conditions.

Condition	Value
$P_{initial}$ (psia)	19.5
$T_{initial}$ (K)	21.366
$U_{initial}$ (m/s)	0.0, 0.0, 0.0

Material Properties

Fluid properties for the liquid and vapor phases were set to constant values at the initial saturation temperature except the density property. For the liquid, the density was modeled as a cubic function of temperature to account for natural convection. STAR-CCM+ does not have a Boussinesq approximation model compatible with the Volume-of-Fluid (VOF) multiphase model. The vapor was modeled as an ideal gas. The surface tension force was modeled via Brackbill et al.⁴ and the constant value used was at the initial saturation temperature. A zero-degree liquid contact angle was used on all internal tank walls. All fluid properties were taken from NIST REFPROP Version 9.1.⁵

The solid tank wall was manufactured out of Aluminum 2219. The solid material properties at cryogenic temperatures are published in Marquardt et al.⁶ Constant values at the initial saturation temperature were used for the Aluminum 2219 properties.

Physics Models

The tank Rayleigh number was on the order of 8×10^{11} , so the $k-\omega$ Menter SST turbulence model was used for this study. A laminar case is of interest but was not carried out for this study. A list of general solver settings is provided in Table 5. The VOF multiphase solver was used to model the two phases.

Table 5. Solver Settings.

Setting	Value/Method
Time step (s)	0.005
Transient Solver	Implicit Unsteady
Temporal Discretization	1st Order
Flow Solver	Segregated
Flow Convection Discretization	2nd Order
Volume Fraction Convection Discretization	HRIC
Energy Discretization	2nd Order
Turbulence Model	$k-\omega$ Menter SST

The VOF transition boiling model was used to model the boiling at the wetted walls. The transition boiling model aims to match the wall boiling heat flux as a function of wall superheat through the nucleate and transition boiling regimes. Wall superheat, or excess temperature, is defined in Eq. (1).

$$\Delta T_{sup} = T_{wall} - T_{sat} \quad (1)$$

The wall heat flux is defined in a piecewise manner shown in Figure 9³. Experimental data for pool boiling of LH2 on a horizontal wall in microgravity were taken from Reference 7. The curve fit and digitized experimental data are plotted in Figure 10 with the chosen parameter values listed in Table 6. The curve fit does not capture the film boiling regime heat flux because the convective

and radiative heat fluxes, which are dominant in the film boiling regime, are not accounted for in the piecewise approximation. The convective heat flux is inherently captured by solving the flow and energy equations simultaneously. Radiation is not considered in this study. Film boiling was not expected to occur during the venting process.

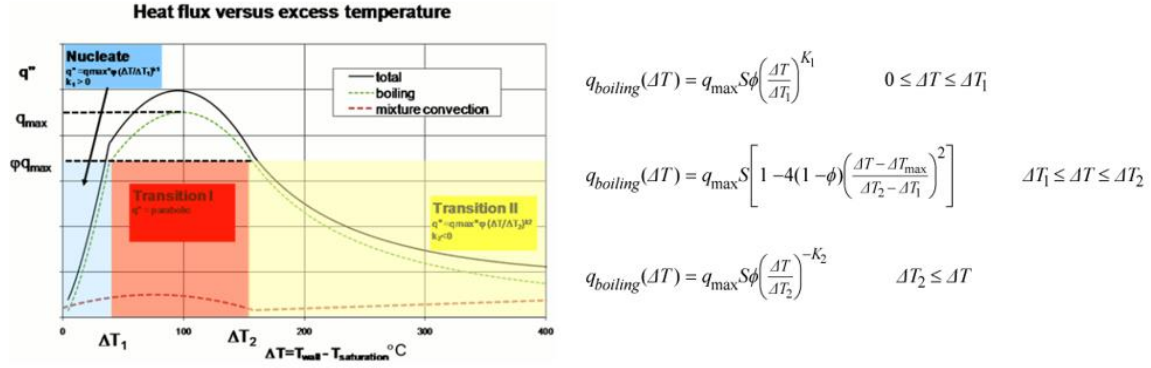


Figure 9. Piecewise Definition of Boiling Curve for STAR-CCM+ VOF Transition Boiling Model.³

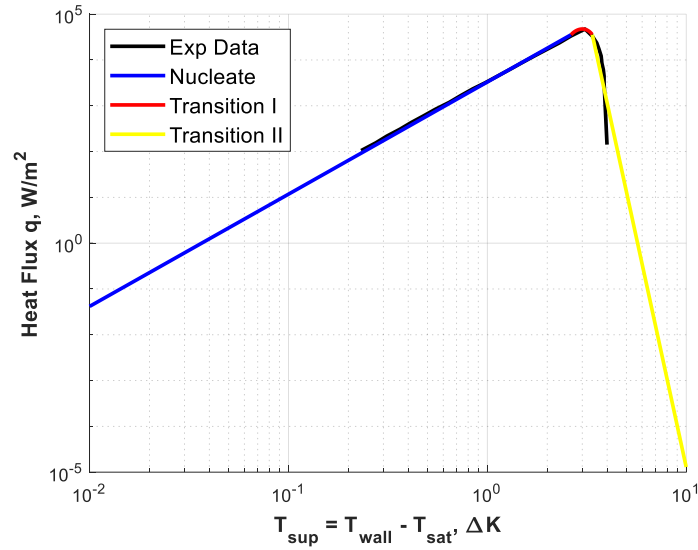


Figure 10. Piecewise Curve Fit for LH2 Boiling Curve with $a/g = 10^{-6.7}$

Table 1. Piecewise Boiling Curve Parameters for LH2 Boiling in Microgravity.

Parameter	Value
q_{max} (kW/m ²)	47.351
$k1$	2.45
$k2$	20.0
$\Delta T1$ (K)	2.6343
$\Delta T2$ (K)	3.3704
S	1.0
ϕ	0.75

For the transition and nucleate regimes, the boiling mass transfer over the area that nucleation sites cover is defined by Eq. (2) where h_{lat} is the latent heat and C_{ew} is an evaporation boiling coefficient that defines the percentage of the boiling heat flux that is used for the generation of vapor. It is related to the probability of forming boiling bubbles from nucleation sites that develop on the heated wall. This serves as a limiter to how many nucleation sites turn into bubbles and all the uncertainties in bubble formation (surface roughness, contact angle, etc.) are lumped into this constant. The constant can be tuned and is dependent on problem definition. The heat and mass transfer is applied to the computational cells next to the solid wall boundary. Interfacial mass transfer was modeled using the Schrage relation defined in Eq. (3) with units of kg/m²s. This model accounts for the interfacial mass transfer at the bulk LVI and the bubble-liquid interfaces. The saturation pressure at the temperature of the cell is defined by the Clausius Clapeyron relation defined in Eq. (4).

$$\dot{m}_{boiling} = \frac{C_{ew} q''_{boiling}}{h_{lat}} \quad (2)$$

$$\dot{m}_i = \left(\frac{2\sigma}{2 - \sigma} \right) \sqrt{\frac{M}{2\pi R T_{cell}}} (P_{sat}(T_{cell}) - P_{abs}) \quad (3)$$

$$P_{sat}(T_{cell}) = P_{ref} \exp \left[\frac{L}{R} \left(\frac{1}{T_{ref}} - \frac{1}{T_{cell}} \right) \right] \quad (4)$$

CFD RESULTS

Interfacial Mass Transfer and Wall Boiling – Effect of Boiling Evaporation Coefficient

The effect of the boiling evaporation coefficient (C_{ew}) on tank pressure and interfacial mass transfer was studied using the coarse mesh. The CFD pressure predictions for various boiling evaporation coefficients are compared to the test data in Figure 11. The boiling evaporation coefficient

has a pronounced effect on the pressure drop predicted by the CFD model. This indicates that the accentuated bend in the test data could be due to vapor generation at the wall and the resulting bulk boiling.

The interfacial mass transfer rates for the various boiling evaporation coefficients are compared in Figure 12. Note that positive is evaporation and negative is condensation. As expected, the $C_{ew} = 0.2$ predicts a higher evaporation rate than $C_{ew} = 0.1$; however, for $C_{ew} = 0.5$, the mass transfer rate is predicted to be lower than the other smaller evaporation coefficients. This is due to condensation occurring inside the much larger bubbles that are predicted by the $C_{ew} = 0.5$ case. This is one challenge presented by using VOF CFD model for this type of problem. To be able to accurately predict the boiling process, the CFD model must resolve the bubbles with sharp interfaces. Here, the larger evaporation coefficient predicts more bubbles that produce larger bubbles by interacting with each other. The CFD model does a poor job of resolving the bubbles so that the inside of the bubble is not pure vapor, but a mixture of liquid and vapor. Therefore, the CFD model predicts condensation of the vapor inside the bubble due to the cooling of the vapor during venting, which reduces the mass transfer rate. If the CFD was able to capture sharper phase gradients and resolve the bubbles more accurately, the model's accuracy would benefit. This requires a denser computational mesh and/or sub-grid models to resolve the interfaces of each bubble more accurately.

Boiling began at seven seconds into the simulation indicated by the curves deviating from the initial rise due to bulk LVI evaporation. The onset of nucleate boiling occurs when the wall superheat reaches $1.0 \Delta K$. A comparison of the bubble sizes for each boiling evaporation coefficient, illustrated by an isosurface of volume fraction equal to 0.5, is presented in Figure 13. The snapshots of the isosurface were taken 50 seconds into the simulation. The predicted bubble size for $C_{ew} = 0.5$ appears to be unrealistically large.

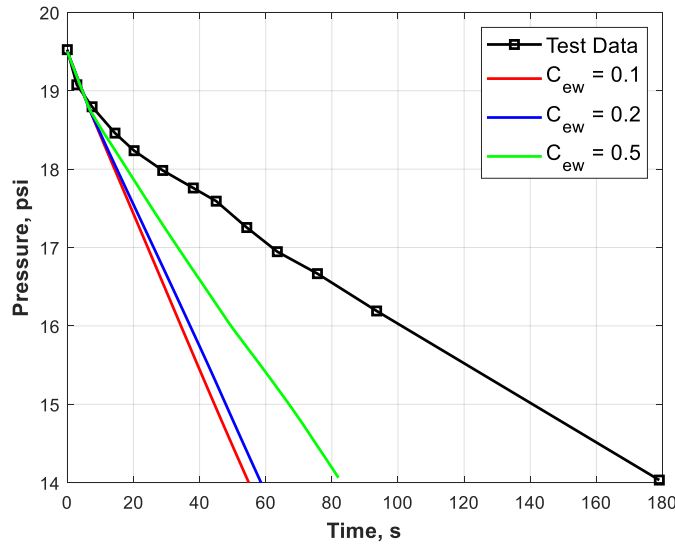


Figure 11. Effect of Boiling Evaporation Coefficient on Tank Pressure.

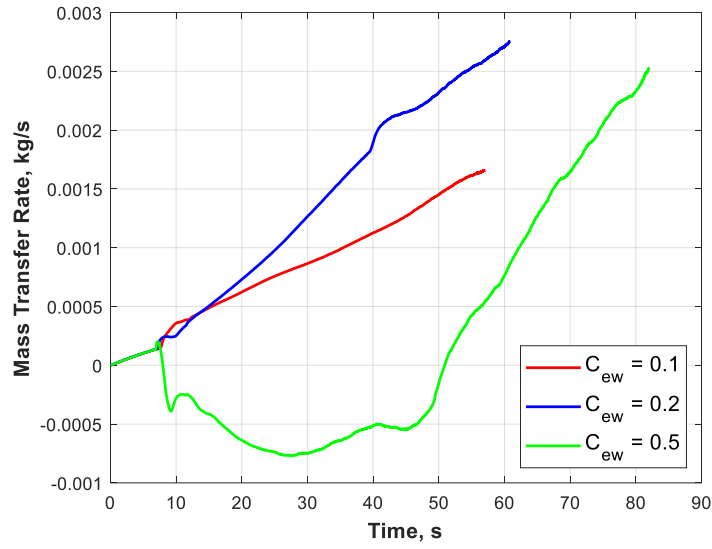


Figure 12. Effect of Boiling Evaporation Coefficient on Interfacial Mass Transfer Rate.



Figure 13. Effect of Boiling Evaporation Coefficient on Bubble Size.

Interfacial Mass Transfer and Wall Boiling – Effect of Boiling Evaporation Coefficient

In the previous section, it was observed that the predicted bubble size increases with increasing boiling evaporation coefficient. There are two mechanisms that are responsible: 1) larger vapor generation rates will produce larger bubbles, and 2) larger bubbles have larger surface areas for

more interfacial mass transfer to occur. Since the liquid is superheated due to venting, the interfacial mass transfer, or bulk boiling, can result in rapid bubble growth while entrained in the liquid. For most practical applications it is not feasible to resolve bubble nucleation, growth, detachment, coalescence, and transport in a CFD simulation.

A study was performed to determine the sensitivity of the bubble size to the mesh/cell size. It was suspected that the CFD simulation will attempt to resolve a bubble with any given mesh, so the bubble size would have a strong correlation to the cell size. This would imply that a mesh-independent solution is not attainable, at least for the phase distribution. The coarse and fine mesh were compared for the $C_{ew} = 0.5$ case. The volume fraction isosurface for each mesh is shown in Figure 14. The snapshots of the isosurface were taken 30 seconds into the simulation. As expected, the finer mesh with smaller cell sizes predicted smaller bubbles. In addition, since the bubble size directly affects the interfacial mass transfer rate and consequently the tank pressure, a mesh-independent solution was not achieved and is likely not possible on a domain of this size using the modeling technique described herein. The results of the tank pressure and mass transfer rate for the two meshes are shown in Figure 15 and Figure 16, respectively.

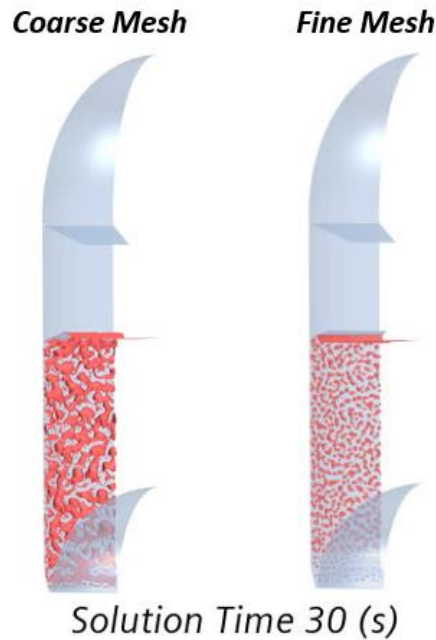


Figure 14. Effect of Mesh Refinement on Bubble Size for $C_{ew} = 0.5$.

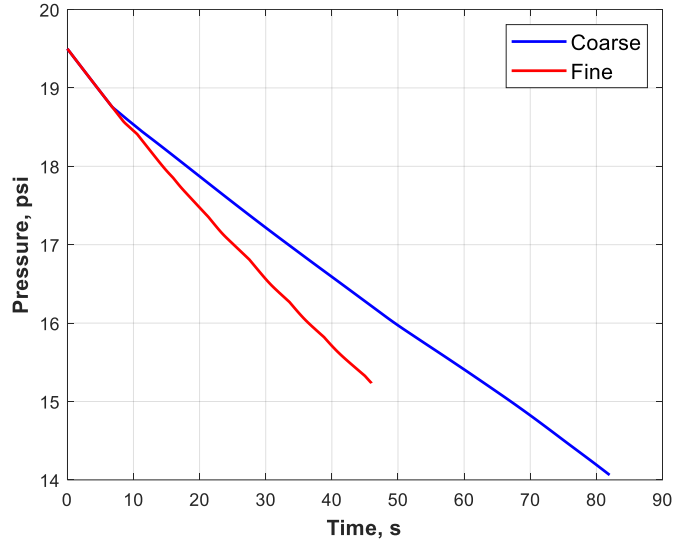


Figure 15. Effect of Mesh Refinement on Tank Pressure for $C_{ew} = 0.5$.

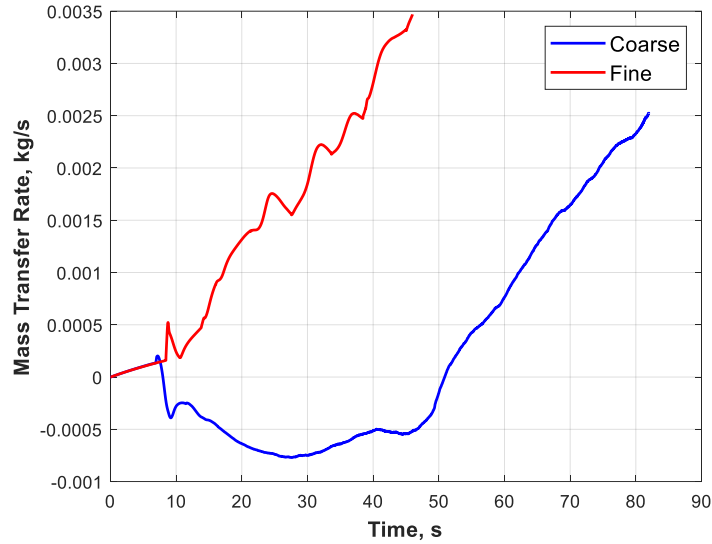


Figure 16. Effect of Mesh Refinement on Interfacial Mass Transfer Rate for $C_{ew} = 0.5$.

Liquid Level Rise Prediction

The effect of applying various settling accelerations on liquid level rise was studied. Figure 17 shows the liquid level rise for a case with no boiling, with boiling with an acceleration of $4e-3 \text{ m/s}^2$, and a case with boiling with a lower acceleration of $1e-3 \text{ m/s}^2$. Without boiling, the liquid level rise is only due to surface tension, where the liquid climbs the wall due to the zero-degree contact angle. For the two cases with boiling, the presence of bubbles cause the LVI to rise above the no boiling case. The lower gravity case ($1e-3 \text{ m/s}^2$) yields a quicker rise of the interface. However, once the LVI nears the end of the baffle, the heights converge and end with similar values. The authors

believe if the baffle was not there to mitigate liquid level rise, the lower gravity case would yield a larger liquid level rise than the $4\text{e-}3 \text{ m/s}^2$ case.

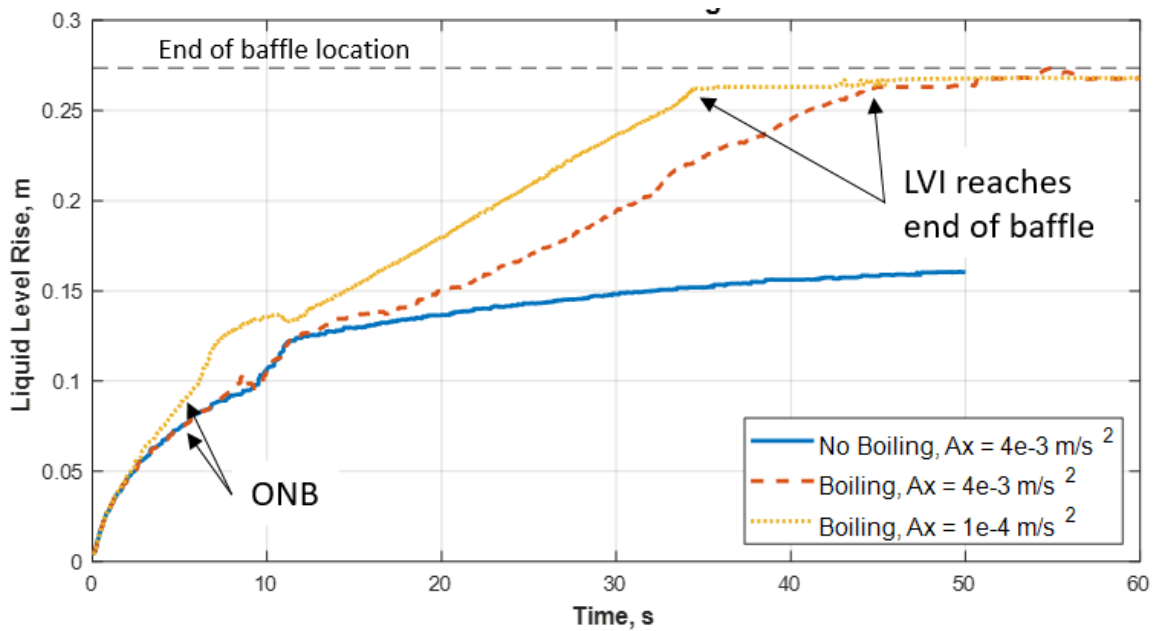


Figure 17. Effect of Settling Acceleration on Liquid Level Rise for $C_{ew} = 0.2$.

CONCLUSION

A CFD model was used to predict the tank pressure drop and liquid level rise in a vented tank subject to low gravity conditions. The CFD model showed strong dependence to the evaporation coefficient in both the tank pressure and phase distribution. In addition, both the tank pressure and phase distribution were shown to be mesh-dependent values. The CFD model presented challenges in modeling the boiling process due to venting the tank below the saturation pressure at the current liquid temperature. The CFD model was unable to resolve the bubbles with sharp interfaces limiting the accuracy of the mass transfer models and phase distribution predictions. In addition, mesh-dependence was shown where the size of the mesh dictated the size of the predicted bubbles. There is a need to improve the accuracy of modeling bubble nucleation, growth, departure, and transport in CFD. Liquid level rise while venting has implications on GN&C for spacecraft, where the settling thrust and unexpected forces on the spacecraft due to venting liquid may be of interest to GN&C spacecraft designers.

ACKNOWLEDGMENTS

The authors recognize Bruce Ciccotosto for performing 2D and 3D simulations of the Saturn AS-203 vent test prior to these studies and extracting all the experimental data from the reports. The authors also recognize the Cryogenic Fluid Management Modeling Project team for their insight, and Matthew Moran for his work on venting models.

REFERENCES

- ¹ Chrysler Corporation Space Division, “Evaluation of AS-203 Low Gravity Orbital Experiment,” NASA-CR-94045, 1967.
- ² Bradshaw, R. D., “Evaluation and Application of Data from Low-Gravity Orbital Experiment, Phase I Final Report,” NASA-CR-109847, 1970.
- ³ Siemens Simcenter STAR-CCM+, Ver. 14.02.010-R8 (2019.1), Plano, TX, 2019.
- ⁴ Brackbill J. U., Kothe, D. B., Zemach, C., “A continuum method for modeling surface tension,” *J. Comp. Phys.* Vol. 100, 1992, pp. 335–354.
- ⁵ NIST REFPROP, Ver. 9.1, Boulder, CO, 2013.
- ⁶ E. Marquardt, J. Le, R. Radebaugh, Cryogenic material properties database, 11th International Cryocooler Conference, Keystone, CO, 2000.
- ⁷ Lei W., Kang Z., Fushou X., Yuan M., Yanzhong L., “Prediction of pool boiling heat transfer for hydrogen in micro-gravity,” *International Journal of Heat and Mass Transfer* Vol. 94, 2016, pp. 465-473.